Journal of Photochemistry and Photobiology A: Chemistry 223 (2011) 157–164

Contents lists available at SciVerse ScienceDirect

Journal of Photochemistry and Photobiology A: Chemistry

journal homepage: www.elsevier.com/locate/jphotochem

Ionic liquid-templated synthesis of mesoporous CeO_2–TiO_2 nanoparticles and their enhanced photocatalytic activities under UV or visible light

Hong Liu*, Mengyang Wang, Yong Wang*, Yuguang Liang, Weiran Cao, Yun Su

Department of Chemical Engineering, Shanghai University, 99 Shangda Road, Shanghai 200444, PR China

ARTICLE INFO

Article history:
Received 1 February 2011
Received in revised form 30 April 2011
Accepted 11 June 2011
Available online 23 August 2011

Keywords:
TiO_2
CeO_2
Mesoporous
Ionic liquid
Photocatalysis
Visible light

ABSTRACT

Mesostructrured CeO_2–TiO_2 nanoparticles with different CeO_2 contents have been successfully synthesized using ionic liquid (1-hexadecane-3-methylimidazolium bromide, $C_{16}MIM^+Br^-$) as a template by a hydrothermal method. The prepared materials were characterized by means of X-ray diffraction (XRD), nitrogen adsorption–desorption, transmission electron microscope (TEM), X-ray photoelectron spectroscopy (XPS) and UV–vis diffuse reflectance spectra analysis. The obtained CeO_2–TiO_2 materials exhibit large specific surface area and uniform pore sizes. Introduction of CeO_2 species can effectively extend the spectral response from UV to visible area and enhance the surface hydroxyl groups of the mesoporous TiO_2. The CeO_2–TiO_2 nanocomposites show high photocatalytic activity in the degradation of the *p*-chlorophenol aqueous solution under the UV or visible irradiation.

1. Introduction

As an important semiconductor material, TiO_2 has been widely used as the photocatalyst because of its chemical and biological inertness, high stability against photocorrosion, non-toxicity, low cost, and excellent degradation for organic pollutants [1,2]. However, practical applications of the TiO_2 are still quite limited, mainly due to the low quantum efficiency and the broad bandgap responding only to UV light [3]. In order to improve the photocatalytic properties of TiO_2, much effort has been made, including transitional metal ion or nonmetal element doping [4,5], codeposition of metals [6] and dye sensitization [7]. Furthermore, TiO_2 combined with another metal oxide, such as SnO_2–TiO_2, WO_3–TiO_2, MoO_3–TiO_2, ZnO–TiO_2, Bi_2O_3–TiO_2, Cu_2O–TiO_2, CeO_2–TiO_2 and ZrO_2–TiO_2 were reported and these mixed metal oxides exhibited a higher photocatalytic degradation rate of pollutants in both gas and aqueous solutions [8–15]. Among them, coupling TiO_2 with cerium oxide attracts much attention because of the special *f* and *d* electron orbital structure and the special properties of CeO_2. It has been found that the variable valences of Ce such as Ce^{4+} and Ce^{3+} make CeO_2 possesses the excellent characteristics in transferring electrons and enhance the light absorption capability in near ultraviolet or ultraviolet [16]. Meanwhile, doping with CeO_2 can double oxygen reserve and transfer capacity of the TiO_2 photocatalysis [17]. Based on the TiO_2 catalytic mechanism [1], the increasing O_2 adsorbed on the surface of particle can easily capture electron, which prohibits the undesirable recombination of electron–hole pair and greatly improves the catalytic oxidation activity.

Design of photocatalysts with mesoporous structure is a promising way to achieve high photocatalytic activity since the ordered mesopore channels facilitate fast intraparticle molecular transfer. Meanwhile, the large surface area may enhance the light harvesting and the adsorption for reactant molecules [14]. Although mesoporous TiO_2 has already been widely studied, only scarce papers concerning the mesoporous CeO_2–TiO_2 have been found in the literature. Yoshikawa et al. [16] synthesized mesoporous CeO_2–TiO_2 nanopowders using a surfactant assisted sol–gel technique. However, the materials synthesized by this method retain very low specific surface area (<100 $m^2\,g^{-1}$) after calcinations. Yu and co-workers [13] reported the synthesis of the thermally stable and ordered mesoporous CeO_2/TiO_2 (Ce/Ti molar ratio = 0.05) using a surfactant P127 as a template by an evaporation-induced self-assembly (EISA) method. However, this synthesis procedure is complicated and the surfactant is environmentally unfriendly.

Recently, room temperature ionic liquids (RTILs) have received considerable attentions in many areas of chemistry and industry due to their superior properties such as high thermal stability, nonflammability, and negligible vapor pressure, etc. More importantly, the self-structuration of RTILs originated from the extended H-bond systems make RTILs suitable as template for the synthesis of inorganic materials with ultrafine nanostructure [18–20]. Compared to

* Corresponding authors. Tel.: +86 21 66137487; fax: +86 21 66137725.
E-mail addresses: liuhong@shu.edu.cn (H. Liu), yongwang@shu.edu.cn (Y. Wang).

1010-6030/$ – see front matter © 2011 Elsevier B.V. All rights reserved.
doi:10.1016/j.jphotochem.2011.06.014

conventional templates, RTILs can be recycled more easily, which is considered to be economical and environmentally friendly. In our preliminary works, mesostructured TiO_2 nanocrystalline with pore size about 3–4 nm have been synthesized in 1-butyl-3-methylimidazolium tetrafluoroborate ($BMIM^+BF_4^-$) ionic liquid by a low temperature hydrothermal method, offering rather high thermal stability and good photocatalytic activity under UV-light irradiation [21]. However, to the best of our knowledge, there was no report about the synthesis of mesoporous mixed metal oxides in RTILs so far.

Herein, we describe a facile synthesis of mesoporous CeO_2–TiO_2 composite with variable Ce/Ti ratios using ionic liquid (1-hexadecane-3-methylimidazolium bromide, $C_{16}MIM^+Br^-$) as a template through hydrothermal method. Such CeO_2–TiO_2 exhibit large specific surface area, uniform pore size and strong spectral response in the visible region. During photocatalytic degradation of *p*-chlorophenol under UV or visible irradiation, the CeO_2–TiO_2 samples reveal high activity compared with pure TiO_2.

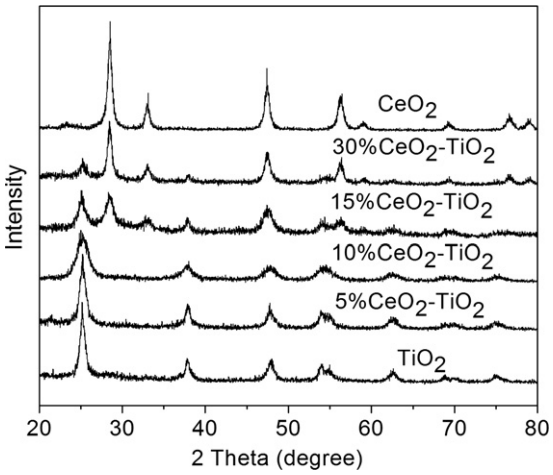

Fig. 1. Wide-angle XRD patterns of CeO_2–TiO_2 with different CeO_2 contents.

2. Experimental

2.1. Synthesis of CeO_2–TiO_2

All the chemicals used were analytically pure. The typical synthesis process was described as following: 0.005 mol of $C_{16}MIM^+Br^-$ was dissolved in 15 ml of distilled water with vigorous stirring at 40 °C for 30 min. Then certain amount of tetrabutyl orthotitanate (TBOT) and $Ce(NO_3)_3$ (total amount of Ti plus Ce is 0.0015 mol) were added into the above solution. The molar proportion of Ce in the composition was varied in the range of 0, 5%, 10%, 15%, 30% and 100%. After stirring for 30 min, pH value was adjusted to 9–10 by dropwise addition of ammonia solution. After stirring for another 2 h, the homogeneous sol was transferred to a 100 ml Teflon-lined stainless steel autoclave at 100 °C for 2 days. Then the product was recovered by filtration, washed thoroughly with deionized water, and dried at 100 °C overnight. The as-synthesized material was calcined in air at 550 °C for 2 h to remove the template.

2.2. Characterization

A Rigaku D/max 2500 diffractometer with Cu Kα (λ = 0.154056 nm) radiation was used for X-ray diffraction (XRD) analysis to determine the crystal phase of CeO_2–TiO_2. Transmission electron microscopy (TEM) and high-resolution TEM images were obtained using a TECNAI 20S-TWIN electron microscope with an energy dispersive spectrum (EDS) analysis facility. Samples were prepared by evaporating very dilute suspensions onto carbon-coated grids. N_2 adsorption–desorption isotherms were obtained at −196 °C on a Micromeritics ASAP 2010 Sorptometer using static adsorption procedures, and the BET surface areas and pore size distributions were calculated by using N_2 adsorption–desorption isotherms. The diffuse reflectance spectra of the samples over a range of 200–800 nm were recorded by a Varian Cary 100 Scan UV–vis system. X-ray photoelectron spectroscopy (XPS) measurement was done with a PHI Quantum 2000 XPS system with a monochromatic Al Ka source and a charge neutralizer. All binding energies were calibrated by using the contaminant carbon (C_{1S} = 284.6 eV) as a reference.

2.3. Photocatalytic activity

The photocatalytic activity of each sample was evaluated in terms of the degradation of *p*-chlorophenol. 0.05 g of photocatalyst was added into an 80 mL quartz photochemical reactor containing 60 ml of 4.7×10^{-4} M *p*-chlorophenol aqueous solution. The mixture was ultrasonic dispersion for 30 min in dark in order to reach the adsorption–desorption equilibrium. A 1000 W tungsten halogen lamp equipped with a UV cutoff filter ($\lambda > 420$ nm) was used as a visible light source and a 250 W high-pressure Hg lamp for which the strongest emission wavelength is 365 nm was used as a UV light source. The lamp was cooled with flowing water in a quartz cylindrical jacket around the lamp, and ambient temperature was maintained during the photocatalytic reaction. At given time intervals, the analytical samples were taken from the mixture and immediately centrifuged and then filtered to remove the particles. The concentration of *p*-chlorophenol was analyzed by checking the absorbance at 225 nm with a UV–vis spectrophotometer (UV-2500, Shimadzu, Japan). The total organic carbon (TOC) was measured using SHIMADZU TOC-VCPH instrument to evaluate the photomineralization degree of *p*-chlorophenol. The photocatalytic behavior of Degussa P25 was also measured as a reference to that of the CeO_2–TiO_2 catalysts in the same conditions.

3. Results and discussion

3.1. Structural characteristics

Fig. 1 shows the wide-angle X-ray powder diffraction patterns of the CeO_2–TiO_2 samples with different amount of CeO_2. The diffraction peaks at 2θ of 25.3°, 36.9°, 38.2°, 38.6°, 48.1°, 53.5°, and 55.6° are attributed to anatase TiO_2 (JCPDF 84-1285). No crystalline phase involving cerium oxide can be observed when the amount of cerium oxide is less than 15%. When the content of $CeO_2 \geq 15\%$, the (1 1 1), (2 0 0), (2 2 0), (3 1 1), (2 2 2), (4 0 0), (3 3 1) and (4 2 0) diffraction peaks of cubic fluorite CeO_2 can be observed. And with increase of cerium content, the peak intensities of cubic fluorite CeO_2 grow and the anatase-phase of TiO_2 become weaker, indicating that the crystallinity of TiO_2 anatase deteriorates and the crystallite size decreases. The diffraction peaks corresponding to cubic fluorite CeO_2 in CeO_2–TiO_2 are also broader and weaker than those in pure cubic fluorite CeO_2. These results indicate that, in comparison with the pure cubic fluorite CeO_2, the crystallinity of cubic fluorite CeO_2 phase deteriorates and the crystallite size becomes finer in CeO_2–TiO_2 mixed oxides. The average crystallite sizes of anatase TiO_2 and cubic fluorite CeO_2 in samples were calculated from the Debye–Scherrer equation using the (1 0 1) diffraction peak of anatase TiO_2 at 25.3° and the (1 1 1) diffraction peak of cubic fluorite CeO_2 at 28.8°, respectively. The results are summarized in Table 1. It can be seen that the average crystalline sizes of both TiO_2 and CeO_2 are finer in the mixed oxides than in the corresponding individual oxides.

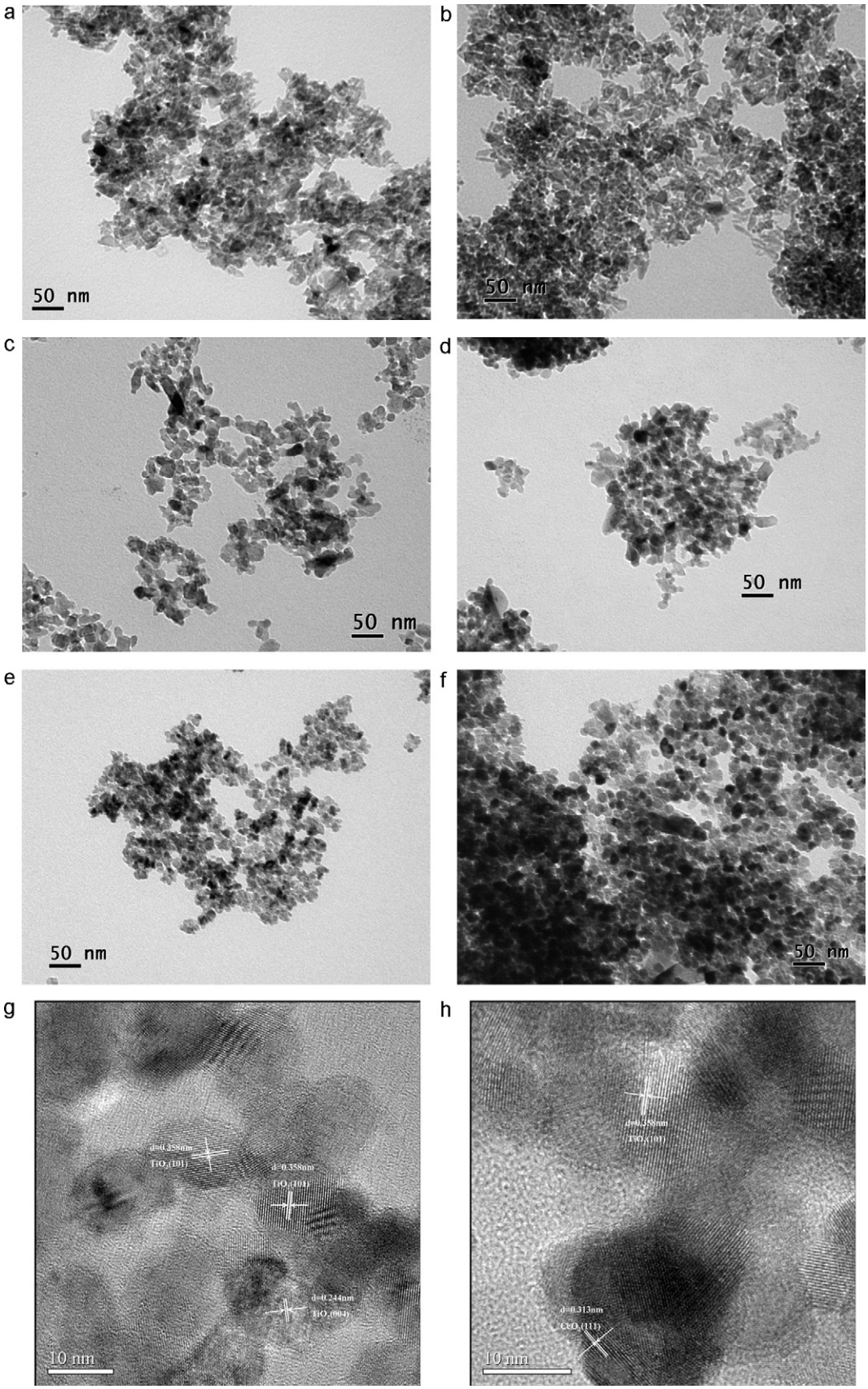

Fig. 2. TEM images of CeO_2–TiO_2 samples with different CeO_2 contents (a: TiO_2; b: 5%CeO_2–TiO_2; c: 10%CeO_2–TiO_2; d: 15%CeO_2–TiO_2; e: 30%CeO_2–TiO_2; f: CeO_2) and HRTEM images of 10%CeO_2–TiO_2 (g) and 15%CeO_2–TiO_2 (h).

Table 1
Properties of CeO_2–TiO_2 with different CeO_2 contents.

Sample	Unit cell parameters			Crystalline size (nm)		S_{BET} ($m^2\ g^{-1}$)	Pore diameter (nm)	Pore volume ($cm^3\ g^{-1}$)
	TiO_2		CeO_2	TiO_2	CeO_2			
	$a=b$ (Å)	c (Å)	$a=b=c$ (Å)					
TiO_2	3.8022	9.5756		15.8		–	–	–
5%CeO_2–TiO_2	3.8057	9.5756		13.7	n.d.[a]	198.3	6.04	0.562
10%CeO_2–TiO_2	3.8059	9.5708		12.7	n.d.	195.8	6.29	0.534
15%CeO_2–TiO_2	3.8086	9.5706		12.4	11.2	180.2	6.54	0.484
30%CeO_2–TiO_2			5.4239	11.2	13.4	150.4	7.04	0.376
CeO_2			5.4128		14.4	–	–	–

[a] Not detected.

Table 1 also shows the unit cell parameters of TiO_2 anatase and cubic CeO_2 in the mixed oxides calculated from the XRD data. TiO_2 anatase belongs to the tetragonal, whose unit cell parameters can be calculated according to the following equations: Bragg's law: $d_{(h\,k\,l)} = \lambda/2\sin\theta$, $1/d^2_{(h\,k\,l)} = (h^2+k^2)/a^2 + l^2/c^2$, where $d_{(h\,k\,l)}$ is the distance between the crystal planes of $(h\,k\,l)$; λ is the wavelength of X-ray used in the experiment; θ is the diffraction angle of the crystal plane $(h\,k\,l)$; and h, k and l are all Miller's indices. In our case, the diffraction peaks from (1 0 1) and (0 0 4) planes of TiO_2 anatase were employed to calculate the unit cell parameters of TiO_2 anatase in the CeO_2–TiO_2 mixed oxides with a content of CeO_2 up to 15%. Using the (1 1 1) diffraction peak, the unit cell parameters of cubic CeO_2 in the CeO_2–TiO_2 mixed oxides with a content of CeO_2 above 30% were calculated according to the equation: $1/d^2_{(h\,k\,l)} = (h^2+k^2+l^2)/a^2$. The unit cell parameters of TiO_2 anatase do not change much from the pure TiO_2 to the CeO_2–TiO_2 mixed oxides, indicating that CeO_2 is present mainly as a separate phase in the CeO_2–TiO_2 sample, i.e., the Ce species are not incorporated into the TiO_2 lattice. This can be attributed to the bigger size of Ce atom (0.97 Å) than that of the Ti atom (0.61 Å), which inhibited the replacement of Ti by Ce in the TiO_2 crystal lattice [22]. The CeO_2 species are highly distributed in the TiO_2, and thus, no significant diffractional peaks indicative of CeO_2 phase can be observed at low CeO_2 amounts (<15%). On the other hand, the unit cell parameters of cubic CeO_2 in CeO_2–TiO_2 are a little bit larger than those in pure CeO_2. This may be attributed to that Ce element existed as a mixture of $Ce^{3+/4+}$ oxidation states in CeO_2–TiO_2, which can be confirmed by the results of XPS shown in Fig. 5. The ionic radius of Ce^{3+} (1.14 Å) is larger than that of Ce^{4+}, so the addition of Ti into CeO_2 contributed to an increase in the lattice parameter. This result concurs with the result reported by Watanabe et al. [23].

The TEM images of CeO_2–TiO_2 samples with different Ce contents are shown in Fig. 2. It is worthy to note that pure TiO_2, 5%CeO_2–TiO_2, 10%CeO_2–TiO_2 and 15%CeO_2–TiO_2 show the rod-like nanoparticles, while pure CeO_2 and 30%CeO_2–TiO_2 indicate spherical particle morphology. It can be observed that the primary particles are relatively uniform and all the sizes of the primary particles are about 15 ± 5 nm, which agrees with the XRD analysis results (Table 1).

The high-resolution TEM images of 10%CeO_2–TiO_2 and 15%CeO_2–TiO_2 are also shown in Fig. 2. As shown in Fig. 2 g, the interplane spacings of 0.358 and 0.244 nm, which correspond to the (1 0 1) and (0 0 4) plane of anatase, respectively, can been seen. No ceria particles can be observed directly in the HRTEM picture, although the existence of Ce is verified by using EDS (not show) and XPS (Fig. 5). This indicates that ceria particles are well dispersed in the 10%CeO_2–TiO_2 sample, which is consistent with the XRD result. For 15%CeO_2–TiO_2 (Fig. 2 h), the d-spacing of 0.313 nm correspond to the (111) plane of cubic fluorite CeO_2 can be observed, demonstrating the existence of the crystal of CeO_2.

Fig. 3 shows the small-angle XRD patterns of CeO_2–TiO_2 samples with different Ce contents. All the samples exhibit a single broad diffraction peak (1 0 0) at low Bragg angle, which indicates clearly the existence of a disordered mesoporous structure [24]. No significant shifts of the diffraction peaks were observed, indicating the presence of CeO_2 had very little influence on the ordering degree of the mesoporous structure.

As shown in Fig. 4, all the CeO_2–TiO_2 samples with the amount of CeO_2 ranging from 5 to 30% display typical type-IV N_2 adsorption–desorption isotherms with H_1 hysteresis, an indicative of mesoporous structure [25]. The pore size distributions demonstrate a narrow pore diameter range. Based on the N_2 adsorption–desorption isotherms, the surface area, pore volume and pore diameter were calculated. As shown in Table 1, both the surface area and pore volume decrease while the pore diameter increase with enhanced Ce-content. In particular, 5%CeO_2–TiO_2 and 10%CeO_2–TiO_2 exhibit higher surface areas than the other CeO_2–TiO_2 mixed oxides.

XPS analysis was conducted to understand the surface chemical state of Ce, Ti, and O in CeO_2–TiO_2 oxides. Ce 3d spectra of CeO_2–TiO_2 mixed oxides are shown in Fig. 5a. The labels used in identifying Ce 3d XPS peaks in Fig. 5a were established by Burroughs et al. [26], where v and u indicate the spin–orbit coupling $3d_{5/2}$ and $3d_{3/2}$, respectively. The peaks referred to as v, v'', and v''' are contributed by CeO_2, and assigned to a mixture of Ce IV ($3d^9 4f^2$) O ($2p^4$), Ce IV ($3d^9 4f^1$) O (2p5) and Ce IV ($3d^9 4f^0$) O ($2p^6$), respectively. The same peak assignment is applied to u structures. The v'/u' doublet is due to photoemission from Ce^{3+} cations. Therefore, a mixture of Ce^{3+}/Ce^{4+} oxidation states exists on the surface of the mesoporous CeO_2–TiO_2 sample. Curve-fitting for the XPS spectra show that the Ce^{3+} concentrations varied from 25.2% in

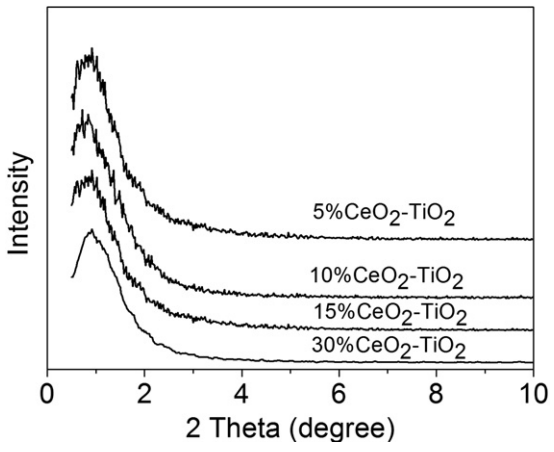

Fig. 3. Small-angle XRD patterns of CeO_2–TiO_2 with different CeO_2 contents.

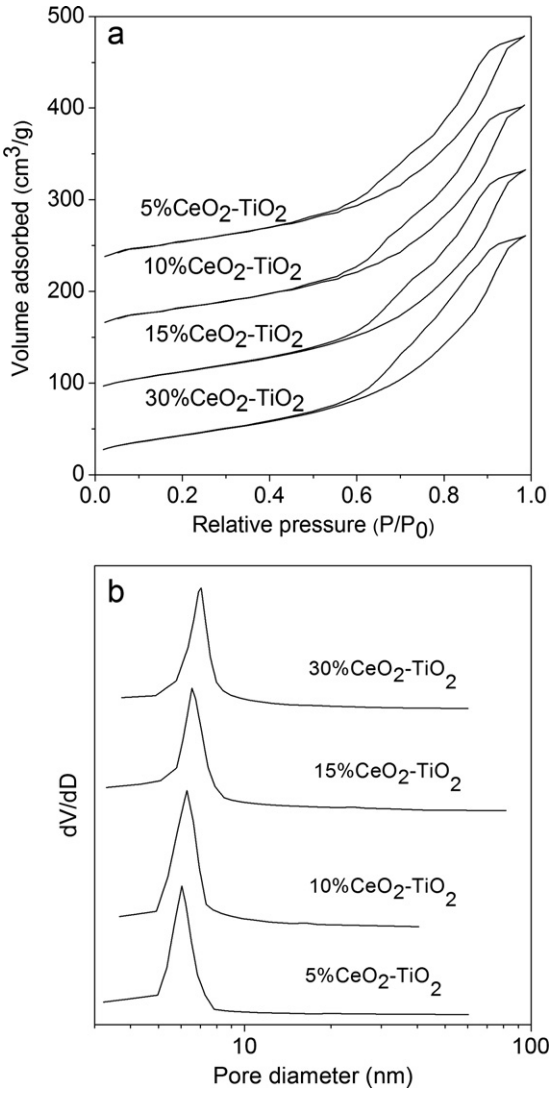

Fig. 4. N_2 adsorption–desorption isotherm (a) and pore size distribution curves (b) of CeO_2–TiO_2.

5%CeO_2–TiO_2 to 9.6% in 30%CeO_2–TiO_2 (Table 2). This suggests that Ce^{3+} concentration of total Ce decrease with increasing amount of CeO_2, which are in good agreement of the studies of Watanabe [23] and Liu et al. [27].

The binding energies of Ti $2p_{1/2}$ and $2p_{3/2}$ in pure TiO_2 are 464.4 and 458.4 eV, respectively (Fig. 5b). These values, along with the sharp features of Ti 2p XPS spectra, indicate that the cations in pure TiO_2 are all in the Ti^{4+} state [13,28]. With the presence of CeO_2, the Ti 2p binding energies do not change much, varying at most within ±0.3 eV, but the Ti 2p XPS peaks broaden. The Ti 2p binding energy of Ti^{3+} is 1.8 eV lower than those of Ti^{4+} [29,30], which is never observed in the Ti 2p XPS spectra of the CeO_2–TiO_2 mixed oxides. This indicates that Ti in the CeO_2–TiO_2 mixed oxides is always in Ti^{4+}, but the heterogeneous environments of Ti^{4+} in the CeO_2–TiO_2 mixed oxides result in the broadening of the Ti^{4+} 2p XPS features [22].

Table 2
Summary of the XPS data for as-prepared samples.

Sample	$Ce^{3+}/(Ce^{3+}+Ce^{4+})$ (%)	O_{OH}/O_T (%)
TiO_2		5.65
5%CeO_2–TiO_2	25.23	5.90
10%CeO_2–TiO_2	20.66	25.53
15%CeO_2–TiO_2	19.27	13.57
30%CeO_2–TiO_2	9.57	7.35

The XPS spectra of O 1s in Fig. 5c are wide and asymmetric; the left side is wider than the right from the figure, indicating that at least two kinds of oxygen species are present at the surface, which can be recognized by resolving XPS curves. The dominant peak at about 529.6 eV is a characteristic of metallic oxides, which is in agreement with O 1s electron-binding energy arising from the ceria and titania lattice. While the signal at 532.0 eV can be associated to surface hydroxyl groups [13,22]. Based on the area integral of the two peaks corresponding to lattice oxygen (OL) and surface hydroxyl (OOH) of O 1s photoemissions, the ratio of OOH to OT (OT = OOH + OL) for all samples was calculated as shown in Table 2. It can be noticed that the introduction of CeO_2 species can effectively enhance the surface hydroxyl groups on the surface of the mesoporous TiO_2. The highest surface concentration of hydroxyls appears for the 10%CeO_2–TiO_2 mixed oxide.

3.2. Optical properties

UV–vis diffuse reflectance spectra (DRS) of TiO_2, CeO_2 and the CeO_2–TiO_2 samples are plotted in Fig. 6a. The results reveal that the pure TiO_2 displays no significant absorbance for visible lights due to the large energy gap of TiO_2. The CeO_2–TiO_2 samples show spectral response in the visible region (λ = 400–600 nm) owing to the photosentisizing effect of CeO_2 and the absorbance become stronger with the increase of Ce content from 5 to 10%. However, further increase of the Ce content leads to a weaker light absorbance. This can be attributed to the fact that the excessive ceria (≥15%) may result in agglomeration of CeO_2 nanoparticles, which will reduce its photosentisizing effect, leading to the poor harvesting for visible lights [14]. The 10%CeO_2–TiO_2 sample exhibits a much stronger absorption in both ultraviolet and visible-light regions than that of other CeO_2 doped samples. The band energy gap of the as-prepared samples could be calculated by using $(\alpha h\upsilon)^n = k(h\upsilon - E_g)$, where α is the absorption coefficient, k is the parameter that related to the effective masses associated with the valence and conduction bands, n is 1/2 for a direct transition, $h\upsilon$ is the absorption energy, and E_g is the band gap energy [31,32]. Plotting $(\alpha h\upsilon)^{1/2}$ versus $h\upsilon$ based on the spectral response in Fig. 6a give the extrapolated intercept corresponding to the E_g value (see Fig. 6b). As shown in Table 3, the CeO_2–TiO_2 samples exhibit decreased E_g values (2.36, 2.30, 2.42 and 2.50 eV, respectively) with respect to that of TiO_2 sample (3.18 eV), indicating that the enhanced ability to absorb visible-light of the CeO_2–TiO_2 samples. This can be explained as follows: there are different bandgap between TiO_2 (3.18 eV) and CeO_2 (2.88 eV). When coupling CeO_2 with TiO_2, the energy bands of two semiconductors will overlap and bend, this can result in the formation of new energy levels in CeO_2–TiO_2, leading to the decrease of bandgap. Table 3 also shows that the E_g value of CeO_2–TiO_2 decreases with the increase of Ce content from 5 to 10%. However, the E_g value increases slightly with further increase of the Ce content.

3.3. Photocatalytic activity

In order to explore the photocatalytic activity of the CeO_2–TiO_2 samples, the degradation of *p*-chlorophenol aqueous solution was carried out under UV and visible-light irradiation. It is found that the blank experiment, in the absence of catalyst, exhibits negligible degradation (Fig. 7). The data displayed in Fig. 7 clearly indicate that CeO_2 doped TiO_2 samples exhibit higher photocatalytic activity under UV irradiation than pure TiO_2 as well as pure CeO_2, suggesting that CeO_2 addition can enhance the photocatalytic activity of pure TiO_2. Moreover, the CeO_2-modified TiO_2 samples show a much

Table 3
The energy of the band gap (E_g) of CeO_2–TiO_2 with different CeO_2 contents.

Sample	TiO_2	5%CeO_2–TiO_2	10%CeO_2–TiO_2	15%CeO_2–TiO_2	30%CeO_2–TiO_2	CeO_2
E_g (eV)	3.18	2.36	2.30	2.42	2.50	2.88

higher level of activity than that of Degussa P25. The existence of mixture of Ce^{3+}/Ce^{4+} oxidation states on the surface of CeO_2–TiO_2, which can be known from XPS analysis (Fig. 5), denote the metal composite is not fully oxidized, so that Ce^{4+} can easily capture electrons and prevent the combination of photo-generated electrons and holes, resulting in a higher quantum efficiency of photocatalytic reaction [33]. Secondly, the photo-induced electrons in the TiO_2 can drift to the CeO_2 under the inner electric field between CeO_2 and TiO_2 due to the energy band bending in space charge region. It is more helpful for the separation of photoinduced electron–hole pairs in TiO_2, resulting in the improvement of photocatalysis under UV illumination [27]. In addition, with the doping of CeO_2, the abundant surface hydroxyl groups exist on the surface of TiO_2, which can be attacked by photoinduced holes and yield surface hydroxyl radicals with high oxidation capability [13,34].

The photocatalytic degradation rate of *p*-chlorophenol and the mineralization rate on the as-prepared samples under visible irradiation are shown in Fig. 8. It demonstrates that the pure TiO_2 was inactive since the catalyst could not be activated by visible lights due to a big energy band gap (3.18 eV). Modification of TiO_2 with CeO_2 resulted in abrupt increase of the photocatalytic activity owing to the CeO_2-photosensitization.

From Figs. 7 and 8 it can also be seen that the photocatalytic activity of prepared CeO_2–TiO_2 mixed oxides increases with the increase of Ce content from 5 to 10%. However, the rate of degradation decreases as well as the concentration of sensitizer increases from 15 to 30%. The 10%CeO_2–TiO_2 sample shows the highest photoactivity under both UV and visible-light irradiation, with the degradation rate of 95.3% and 57.5%, respectively. And the mineralization rate under UV and visible-light irradiation for the 10%CeO_2–TiO_2 is 85.3% and 48.9%, respectively. This fact is consistent with its smaller particle size, larger surface area, higher concentration of Ce^{3+}, highest concentration of surface hydroxyl groups, strongest light absorbance and lowest E_g value. This can also be attributed to the fact that when doping content of CeO_2 is low, the CeO_2 particles well dispersed on the TiO_2 surface can act as electron-hole separation centers. On the contrary, when the doping concentration exceeds a certain amount (≥15%), the trap center may become the recombination center of photo-generated electrons and holes. Meanwhile, the excessive ceria result in agglomeration of CeO_2 nanoparticles, which will scatter the incident light, lowering the photoquantum efficiency of the photocatalytic reaction [14].

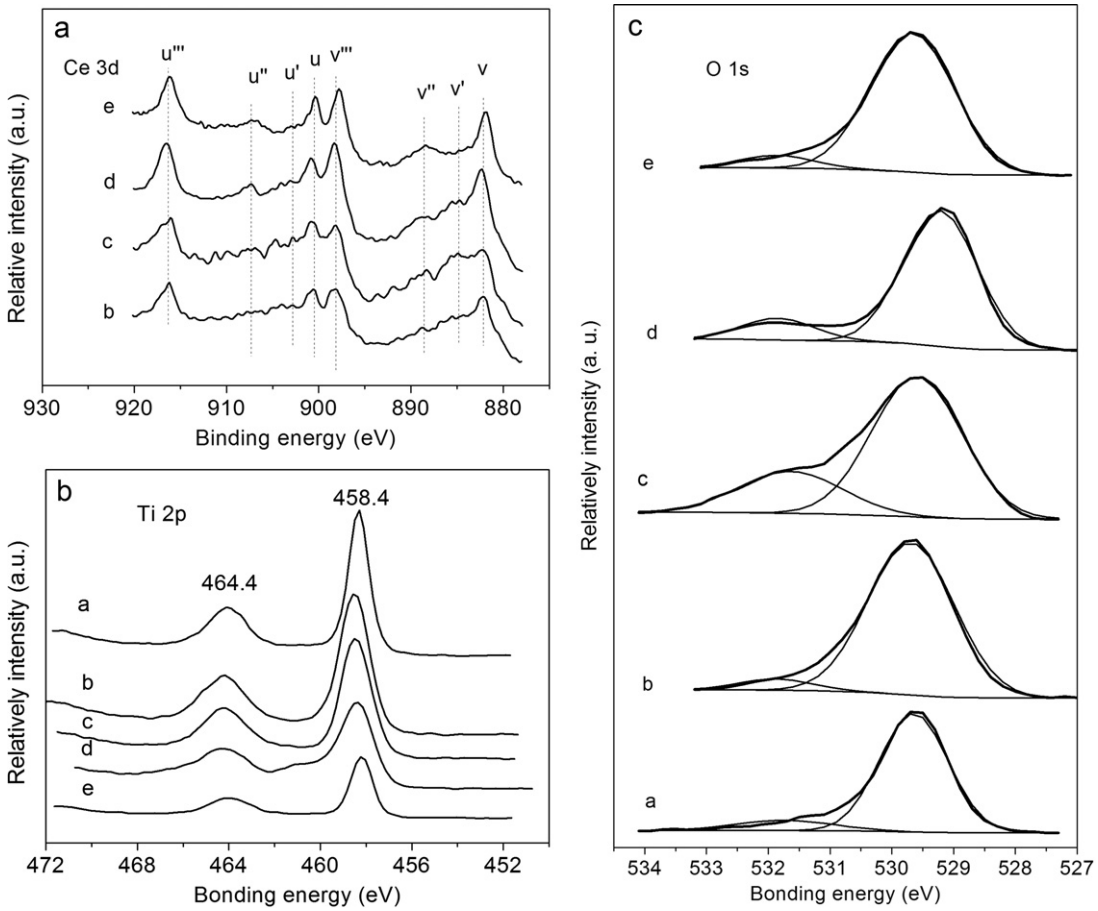

Fig. 5. XPS spectra of CeO_2–TiO_2 (a: TiO_2; b: 5%CeO_2–TiO_2; c: 10%CeO_2–TiO_2; d: 15%CeO_2–TiO_2; e: 30%CeO_2–TiO_2).

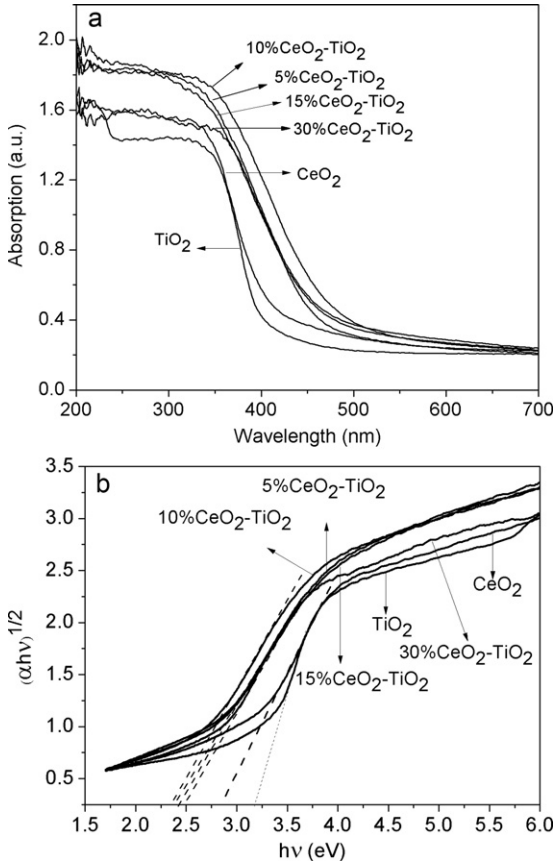

Fig. 6. UV–vis absorption spectra (a) and the optical absorption edges (b) of CeO_2–TiO_2 samples.

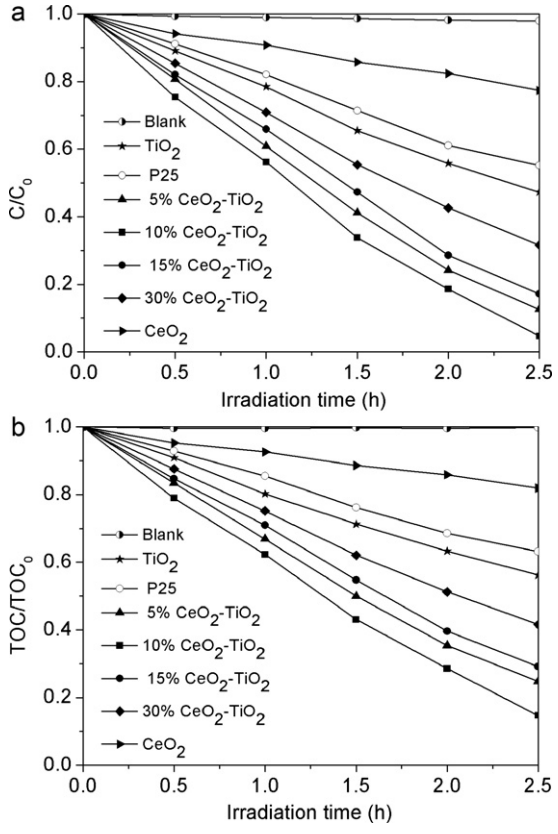

Fig. 7. Photocatalytic degradation rate of *p*-chlorophenol (a) and mineralization rate (b) on CeO_2–TiO_2 catalysts under UV light.

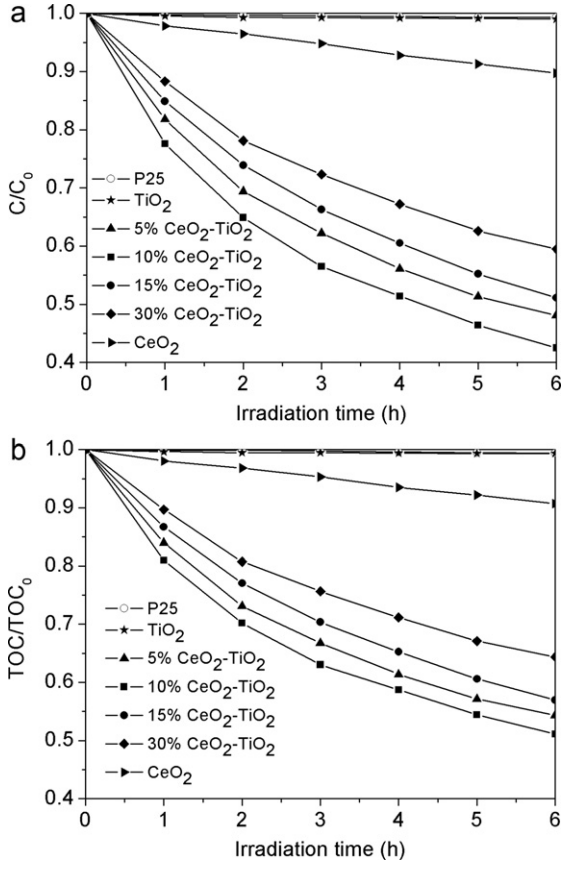

Fig. 8. Photocatalytic degradation rate of *p*-chlorophenol (a) and mineralization rate (b) on CeO_2–TiO_2 catalysts under visible light.

4. Conclusions

Mesostructrured CeO_2–TiO_2 nanocomposites with large specific surface area and uniform pore size have been successfully synthesized using ionic liquid ($C_{16}MIM^+Br^-$) as a template by a facile hydrothermal method. Well-crystallized CeO_2–TiO_2 could be obtained and the crystal size was ~11–16 nm for the samples with different Ce/Ti molar ratios. At least two kinds of oxygen species were present on the particle surface from XPS investigation. The Ti element mainly existed as a chemical state of Ti^{4+} and Ce element existed as a mixture of $Ce^{3+/4+}$ oxidation states. The CeO_2–TiO_2 samples showed strong spectral response in the visible region and exhibited high photocatalytic activity under UV or visible irradiation compared with pure TiO_2.

Acknowledgments

The authors gratefully acknowledge Shanghai Municipal Commission of Education (11YZ15), Shanghai Leading Academic Disciplines (S30109), National Natural Science Foundation of China (50971085), Shanghai Science & Technology Committee (09JC1406100) and the Program for Professor of Special Appointment in Shanghai (Eastern Scholar) for the financial support.

References

[1] A.L. Linsebigler, G. Lu, J.T. Yates, Photocatalysis on TiO_2 surfaces: principles, mechanisms, and selected results, Chem. Rev. 95 (1995) 735–758.
[2] R. Asahi, T. Morikawa, T. Ohwaki, K. Aoki, Y. Taga, Visible-light photocatalysis in nitrogen-doped titanium oxides, Science 293 (2001) 269–271.
[3] Y. Zheng, E. Shi, Z. Chen, W. Li, X. Hu, Influence of solution concentration on the hydrothermal preparation of titania crystallites, J. Mater. Chem. 11 (2001) 1547–1551.

[4] H. Yamashita, H. Harada, J. Misaka, M. Takeushi, K. Ikeue, M. Anpo, Degradation of propanol diluted in water under visible light irradiation using metal ion-implanted titanium dioxide photocatalysts, J. Photochem. Photobiol. A: Chem. 148 (2002) 257–261.
[5] J.C. Yu, L. Zhang, Z. Zheng, J. Zhao, Synthesis and characterization of phosphated mesoporous titanium dioxide with high photocatalytic activity, Chem. Mater. 15 (2003) 2280–2286.
[6] W. Wang, J. Zhang, F. Chen, D. He, M. Anpo, Preparation and photocatalytic properties of Fe^{3+}-doped Ag@TiO_2 core–shell nanoparticles, J. Colloid Interface Sci. 323 (2008) 182–186.
[7] F. Chen, W. Zou, W. Qu, J. Zhang, Photocatalytic performance of a visible light TiO_2 photocatalyst prepared by a surface chemical modification process, Catal. Commun. 10 (2009) 1510–1513.
[8] Y. Bessekhouad, D. Robert, J.V. Weber, Photocatalytic activity of Cu_2O/TiO_2, Bi_2O_3/TiO_2 and $ZnMn_2O_4/TiO_2$ heterojunctions, Catal. Today 101 (2005) 315–321.
[9] H. Ohsaki, N. Kanai, Y. Fukunaga, M. Suzuki, T. Watanabe, K. Hashimoto, Photocatalytic properties of SnO_2/TiO_2 multilayers, Thin Solid Films 502 (2006) 138–142.
[10] D.W. Kim, S. Lee, H.S. Jung, J.Y. Kim, H. Shin, K.S. Hong, Effects of heterojunction on photoelectrocatalytic properties of ZnO–TiO_2 films, Int. J. Hydrogen Energy 32 (2007) 3137–3140.
[11] J.H. Pan, W.I. Lee, Preparation of highly ordered cubic mesoporous WO_3/TiO_2 films and their photocatalytic properties, Chem. Mater. 18 (2006) 847–853.
[12] D. Robert, Photosensitization of TiO_2 by M_xO_y and M_xS_y nanoparticles for heterogeneous photocatalysis applications, Catal. Today 122 (2007) 20–26.
[13] G. Li, D. Zhang, J.C. Yu, Thermally stable ordered mesoporous CeO_2/TiO_2 visible-light photocatalysts, Phys. Chem. Chem. Phys. 11 (2009) 3775–3782.
[14] Z. Bian, J. Zhu, S. Wang, Y. Cao, X. Qian, H. Li, Self-assembly of active Bi_2O_3/TiO_2 visible photocatalyst with ordered mesoporous structure and highly crystallized anatase, J. Phys. Chem. C 112 (2008) 6258–6262.
[15] W. Zhou, K. Liu, H. Fu, K. Pan, L. Zhang, L. Wang, C.C. Sun, Multi-modal mesoporous TiO_2–ZrO_2 composites with high photocatalytic activity and hydrophilicity, Nanotechnology 19 (2008) 035610–035616.
[16] S. Pavasupreea, Y. Suzukia, S. Pivsa-Artb, S. Yoshikawa, Preparation and characterization of mesoporous TiO_2–CeO_2 nanopowders respond to visible wavelength, J. Solid State Chem. 178 (2005) 128–134.
[17] T. Morimo, G. Dutta, U.V. Waghmare, T. Baidya, M.S. Hegde, K.R. Priolkar, P.R. Sarode, Origin of enhanced reducibility/oxygen storage capacity of $Ce_{1-x}Ti_xO_2$ compared to CeO_2 or TiO_2, Chem. Mater. 18 (2006) 3249–3256.
[18] Z. Ma, J. Yu, S. Dai, Preparation of inorganic materials using ionic liquids, Adv. Mater. 22 (2010) 261–285.
[19] K. Yoo, H. Choi, D.D. Dionysiou, Ionic liquid assisted preparation of nanostructured TiO_2 particles, Chem. Commun. (2004) 2000–2001.
[20] T. Wang, H. Kaper, M. Antonietti, B. Smarsly, Templating behavior of a long-chain ionic liquid in the hydrothermal synthesis of mesoporous silica, Langmuir 23 (2007) 1489–1495.
[21] H. Liu, Y. Liang, H. Hu, M. Wang, Hydrothermal synthesis of mesostructured nanocrystalline TiO_2 in an ionic liquid–water mixture and its photocatalytic performance, Solid State Sci. 11 (2009) 1655–1660.
[22] J. Fang, X. Bi, D. Si, Z. Jiang, W. Huang, Spectroscopic studies of interfacial structures of CeO_2–TiO_2 mixed oxides, Appl. Surf. Sci. 253 (2007) 8952–8961.
[23] S. Watanabe, X. Ma, C. Song, Characterization of structural and surface properties of nanocrystalline TiO_2–CeO_2 mixed oxides by XRD, XPS, TPR, and TPD, J. Phys. Chem. C 113 (2009) 14249–14257.
[24] S.A. Bagshaw, E. Prouzet, T.J. Pinnavaia, Templating of mesoporous molecular sieves by nonionic polyethylene oxide surfactants, Science 269 (1995) 1242–1244.
[25] K.S.W. Sing, D.H. Everett, R.A.W. Haul, L. Moscou, R.A. Pierotti, J. Rouquerol, T. Siemieniewska, Reporting physisorption data for gas/solid systems, Pure Appl. Chem. 57 (1985) 603–619.
[26] P. Burroughs, A. Hamnett, A.F. Orchard, G. Thornton, Satellite structure in the X-ray photoelectron spectra of some binary and mixed oxides of lanthanum and cerium, J. Chem. Soc., Dalton Trans. 17 (1976) 1686–1698.
[27] B. Liu, X. Zhao, N. Zhang, Q. Zhao, X. He, J. Feng, Photocatalytic mechanism of TiO_2–CeO_2 films prepared by magnetron sputtering under UV and visible light, Surf. Sci. 595 (2005) 203–211.
[28] X. Gao, Y. Jiang, Y. Zhong, Z. Luo, K. Cen, The activity and characterization of CeO_2–TiO_2 catalysts prepared by the sol–gel method for selective catalytic reduction of NO with NH_3, J. Hazard. Mater. 174 (2010) 734–739.
[29] Z. Zhang, V.E. Henrich, Electronic interactions in the vanadium/TiO_2 (1 1 0) and vanadia/TiO_2 (1 1 0) model catalyst systems, Surf. Sci. 277 (1992) 263–272.
[30] N.J. Price, J.B. Reitz, R.J. Madix, E.I. Solomon, A synchrotron XPS study of the vanadia–titania system as a model for monolayer oxide catalysts, J. Electron Spectrosc. Relat. Phenom. 98–99 (1999) 257–266.
[31] M. Yoon, M. Seo, C. Jeong, J.H. Jang, K.S. Jeon, Synthesis of liposome-templated titania nanodisks: optical properties and photocatalytic activities, Chem. Mater. 17 (2005) 6069–6079.
[32] X. Peng, G. Meng, J. Zhang, L. Zhao, X. Wang, Y. Wang, L. Zhang, Electrochemical fabrication of ordered Bi_2S_3 nanowire arrays, J. Phys. D: Appl. Phys. 34 (2001) 3224–3328.
[33] H. Yang, K. Zhang, R. Shi, Sol-gel synthesis and photocatalytic activity of CeO_2/TiO_2 nanocomposites, J. Am. Ceram. Soc. 90 (2007) 1370–1374.
[34] C.S. Turchi, D.F. Ollis, Photocatalytic degradation of organic water contaminants: mechanisms involving hydroxyl radical attack, J. Catal. 122 (1990) 178–192.